Influence of collision cascade statistics on pattern formation of ion-sputtered surfaces

M. Feix, A. K. Hartmann,* and R. Kree†

Institut für Theoretische Physik, Universität Göttingen, Göttingen, Germany

J. Muñoz-García‡ and R. Cuerno§

Departamento de Matemáticas and Grupo Interdisciplinar de Sistemas Complejos (GISC), Universidad Carlos III de Madrid,
Avenida de la Universidad, 30, 28911 Leganés, Spain

Theoretical continuum models that describe the formation of patterns on surfaces of targets undergoing ion-beam sputtering are based on Sigmund's formula, which describes the spatial distribution of the energy deposited by the ion. For small angles of incidence and amorphous or polycrystalline materials, this description seems to be suitable, and leads to the classic Bradley and Harper (BH) morphological theory [R. M. Bradley and J. M. E. Harper, J. Vac. Sci. Technol. A **6**, 2390 (1988)]. Here we study the sputtering of Cu crystals by means of numerical simulations under the binary-collision approximation. We observe significant deviations from Sigmund's energy distribution. In particular, the distribution that best fits our simulations has a minimum near the position where the ion penetrates the surface, and the decay of energy deposition with distance to ion trajectory is exponential rather than Gaussian. We provide a modified continuum theory which takes these effects into account and explores the implications of the modified energy distribution for the surface morphology. In marked contrast with BH's theory, the dependence of the sputtering yield with the angle of incidence is nonmonotonous, with a maximum for nongrazing incidence angles.

I. INTRODUCTION

Ion bombardment of solids often gives rise to characteristic surface topographies, which evolve under stationary and homogeneous ion fluxes. Besides kinetic roughening, wavelike ripple structures may occur. Such height modulations on the submicron scale have been observed for crystalline semiconductors[1,2] as well as for crystalline metals[3,4] and some amorphous[5] and polycrystalline materials, see a recent review in Ref. 6. According to continuum theories, which are based on the work of Bradley and Harper (BH),[7] the periodic patterns emerge from a competition between a roughening curvature instability due to characteristics of the spreading of ion energy, and simultaneous smoothing processes due to surface diffusion.[8,9] Although this mechanism seems to be quite universal, there are material-specific differences in the evolution of surface topographies. For nonmetallic substrates, for example, one usually needs off-normal incidence of ion flux to produce ripples, which change their orientation with the incidence angle,[2,4,5,10–14] whereas ripples are observed on metallic substrates even at normal incidence, and the orientation of ripples changes with substrate temperature.[3,15,16] Furthermore, the smoothing mechanism of surface diffusion is not well understood yet. In previous simulations,[17] we have found that the emerging patterns depend crucially on the diffusion mechanisms applied. In particular the long-time behavior, which is governed in the continuum theory by nonlinear terms, depends even qualitatively on the surface diffusion mechanism. Given that the surface topographies resulting from different mechanisms of surface diffusion have been studied by simulations elsewhere,[18] in the present work we will focus on specificities due to the energy deposition process.

Continuum theories for the surface morphology of the target usually assume that the kinetic energy of an ion hitting a solid surface spreads in the bulk and produces a Gaussian density of deposited energy

$$\epsilon_s(\mathbf{r}) = N_s \epsilon e^{-[(x^2+y^2)/2\beta^2]} e^{-[(z+\bar{a})^2/2\alpha^2]},$$

$$N_s = [(2\pi)^{3/2}\alpha\beta^2]^{-1}, \tag{1}$$

where $\mathbf{r} = (x, y, z)$ is a point within the target, ions are falling along the $\hat{\mathbf{z}}$ axis and penetrate an average distance $\bar{a}$ within the solid, ϵ is the average kinetic energy carried by each ion, and the values of α, β describing the spreading of the energy are of the same order of magnitude as $\bar{a}$. The Gaussian form (1) is based on the work of Sigmund,[19] who considered a polycrystalline or amorphous target and analyzed the kinetic transport theory of the sputtering process. He found that in the elastic collision regime at energies where electronic stopping is not dominating, the deposited energy can be approximated by a Gaussian near its maximum. The quality of the approximation is reasonable, if mass differences between substrate and ion are not too large. Obviously, the Gaussian form is not universal and consequences of deviations from the Gaussian form within the BH model have not been studied yet. In particular, although the observations of ripples on single crystalline metals[3,15,16,20] are qualitatively described by the BH model, the latter is strictly a theory for amorphous materials, and thus there is a need to justify theoretically the emergence of such type of patterns onto this other class of substrates.

Obtaining more detailed information about the deposited energy from simulations has become straightforward by now, as there are many well calibrated, efficient simulation methods for ion impact available.[21–25] In the present work, we use simulations based on the binary-collision approx-

imation[23,25,26] and consider a metallic material (Cu), for which we generate statistical ensembles of collision cascades emerging from single-ion impact events on flat surfaces. In previous work on the simulation of sputtering in metals, already some deviations[27–30] from Sigmund's theory have been found. In particular they are due to the directional anisotropy of the collision cascades, which follow closed packed planes of atoms (called "focusing").[31] Anyway, in those references the analysis of the data was performed as a function of depth but not as a function of the lateral distance. Also the angular distributions of the ejected atoms has been evaluated,[32–34] again without an analysis as a function of the lateral distance. In one work,[35] full ejection patterns of atoms were actually studied (at zero temperature), but no quantitative analysis was performed apart from measuring the sputter yield. To compare with Eq. (1), we analyze here our data also in terms of the lateral distribution of the deposited energies and ejected particles. We do not claim to perform the best state of the art simulation of ion impact on Cu (for example, we only consider a very crude model of surface binding forces). Rather, we aim at more generic results, which are of relevance to the theory of surface evolution. Our simulations provide an average density of deposited energy, which is quite different from the Gaussian form in Eq. (1). We furthermore consider the fluctuations around this average and find strong, intrinsic noise. In the subsequent part of our work we investigate the consequences of the simulation results for the continuum theory of pattern formation by ion-beam sputtering. We obtain that the modified energy distribution obtained in the numerical simulations induces a sputtering yield that overcomes some of the shortcomings (when comparing with experiments) of the analogous result within BH's theory. Moreover, we recover the production of the ripple instability, and the dependence of the pattern features with phenomenological parameters similar to BH theory, thus providing a theoretical framework within which observations of ripples on metals can be naturally accomodated.[3,15,16,20]

II. OBSERVABLES OF CASCADE STATISTICS

In this section we want to relate observables of our simulations to the phase space density

$$g(\mathbf{v}, \boldsymbol{\rho}, z, t | \boldsymbol{\rho}_0, z = 0, \mathbf{v}_0, t = 0), \qquad (2)$$

where $\boldsymbol{\rho} \equiv (x, y)$. This function is the basic quantity underlying the kinetic theory of collision cascades, and also introduces the quantities which are used in the construction of a continuum theory of surface pattern formation by ion bombardment. Function g is the average density of cascade particles in six-dimensional $(\mathbf{v}, \boldsymbol{\rho}, z)$ space at time t, under the assumption that one ion has hit the surface at $\boldsymbol{\rho}_0$ and at $t = 0$ with velocity $\mathbf{v}_0$. As we will only treat identical initial conditions with $\boldsymbol{\rho}_0 = 0$ and $\mathbf{v}_0 = -|\sqrt{2\epsilon_0/m}|\mathbf{e}_z$, we will use the abbreviated notation $g(\boldsymbol{\rho}, z, \mathbf{v}, t)$ and drop the explicit dependence on $\boldsymbol{\rho}_0$ and $\mathbf{v}_0$. The average has to be taken over an ensemble of targets, which differ by random, thermal displacements of atoms.

To define our simulation observables in terms of the phase space density, first note that $g(\boldsymbol{\rho}, z, \mathbf{v}, t)(\mathbf{v} \cdot d\mathbf{a}) \, d^3\mathbf{v} \, dt$ is the number of particles, which penetrate a surface element $d\mathbf{a}$ situated at position $(\boldsymbol{\rho}, z)$, with velocity $\mathbf{v}$ during the time interval dt. The phase space density and the corresponding current density may as well be considered as functions of position, energy and direction of velocity using $\mathbf{v} = \sqrt{2\epsilon/m} \hat{\mathbf{v}}$, $\hat{\mathbf{v}}$ being the unit vector in the direction of $\mathbf{v}$, so that $\mathbf{v} d^3\mathbf{v} = (2/m^2)\epsilon\hat{\mathbf{v}} \, d\epsilon \, d\hat{\mathbf{v}}$. The current density $\mathbf{j}(\epsilon, \boldsymbol{\rho}, z, t)d\epsilon$ of cascade particles of energy near ϵ is given by

$$\mathbf{j}(\epsilon, \boldsymbol{\rho}, z, t)d\epsilon = \frac{2}{m^2}d\epsilon \int d\hat{\mathbf{v}} \, \epsilon\hat{\mathbf{v}} g(\epsilon, \hat{\mathbf{v}}, \boldsymbol{\rho}, z, t). \qquad (3)$$

From Eq. (3), it is obvious that the time integral

$$h_{2d}(\epsilon, \boldsymbol{\rho}, z)dx \, dy = \int_0^\infty dt \mathbf{e}_z \cdot \mathbf{j}(\epsilon, \boldsymbol{\rho}, z, t)dx \, dy \qquad (4)$$

equals the total average number of particles per energy at energy ϵ of a single collision cascade, which penetrate the surface element $dx \, dy\mathbf{e}_z$ located at $(\boldsymbol{\rho}, z)$. Note that h_{2d} is a surface density and the quantities

$$n_{2d}(\boldsymbol{\rho}, z) = \int_0^\infty d\epsilon \, h_{2d}(\epsilon, \boldsymbol{\rho}, z) \qquad (5)$$

and

$$\epsilon_{2d}(\boldsymbol{\rho}, z) = \int_0^\infty d\epsilon \, \epsilon h_{2d}(\epsilon, \boldsymbol{\rho}, z) \qquad (6)$$

give, respectively, the average number of particles and average energy per surface area transported to the (xy) plane at z by the collision cascade.

The particles arriving at the $z = 0$ plane (which constitutes the surface of the material) with velocities in outward direction will leave the bulk if they overcome the surface binding forces. We will use a simple spherical barrier model of surface binding with barrier height U. This implies that all particles arriving at the surface with kinetic energy $\epsilon > U$ will be sputtered off. The surface density n_U of these particles is therefore given by Eq. (5) with the lower boundary of the ϵ integration replaced by U. The total sputtering yield is the surface integral of this density, $Y_U = \int d^2\boldsymbol{\rho} \, n_U(\boldsymbol{\rho})$. At internal surfaces there is no surface binding and thus

$$p(\epsilon, \boldsymbol{\rho}, z) = h_{2d}(\epsilon, \boldsymbol{\rho}, z)/Y_{U=0} \qquad (7)$$

becomes the probability density to find a particle with energy ϵ crossing the internal surface at location $(\boldsymbol{\rho}, z)$, and $p_U(\boldsymbol{\rho}) = n_U(\boldsymbol{\rho})/Y_U$ is the probability density to find a particle leaving the bulk at $\boldsymbol{\rho}$. These are the quantities we will study in the subsequently described simulations.

III. BINARY-COLLISION APPROXIMATION SIMULATIONS

Atomic displacements and particle ejection from a solid due to the impact of a single ion with kinetic energy in the keV range can be simulated by using the binary-collision

approximation[25] (BCA). The basic idea is to substitute the detailed particle trajectories by trajectories where the particles travel with constant velocity until they "hit" onto another particle. Each collision event is integrated analytically or numerically, leading to new positions and velocities of the particles participating in the collision. Hence, the full dynamical process is reduced to a cascade of binary collisions. For a full description of the algorithm, which follows standard implementations, we refer to the literature.[23] Nevertheless, for the convenience of the reader, we provide some details.

(1) The code allows for arbitrary positions of the bulk atoms. Here, the positions of the atoms making up the undisturbed solid were displaced from ideal lattice sites of a Cu single crystal (170 000 atoms of an fcc structure with lattice constant 3.61 Å, corresponding to a solid of 10.6 nm $\times$ 10.6 nm and a bulk depth of 18 nm) by uncorrelated, Gaussian distributed displacements (standard deviation 0.16 Å) to account for thermal fluctuations.

(2) Our program is suitable for studying defect accumulation during multiple impact, but this feature is not used in the present work. Hence, the change of the target structure during ion irradiation is neglected.

(3) All model parameters of the algorithm have been adjusted to Cu projectiles of a few keV, hitting a Cu single crystal.[36]

(4) Each cascade is started by shooting one ion onto the crystal. Hence, initially each collision cascade consists of only the ion.

(5) For each ion of an ensemble, an additional homogeneous lateral random displacement was added, which was taken to be uniformly distributed within a square of edge length 1 lattice constant. Thus, within every ensemble the ion hits upon macroscopically identical but microscopically differing configurations of the solid.

(6) Prior to the collisions, all target atoms are assumed to be at rest.

(7) Each projectile travels with constant velocity, until an interaction occurs. A projectile/target interaction was assumed to take place if the impact parameter was less than $p_{max} = 2.6$ Å.

(8) The interaction was modeled using a screened Coulomb potential, where the screening function we used was given by Moliere.[37]

(9) To model electronic stopping, we applied inelastic scattering following Refs. 23 and 38.

(10) Due to this choice of the potential/electronic stopping, the collisions had to be integrated numerically, and the results were stored as a function of the energy and of the impact parameter.

(11) After the collision, target atoms exceeding the binding energy $E_b = 3.5$ eV are added to the collision cascade, carrying an energy after the collision, that is reduced by E_b. For simplicity, we used the same value as for the surface binding energy, i.e., $E_s = 3.5$ eV.

(12) Cascade particles having an energy below $E_c = 2.0$ eV are removed from the cascade, because they cannot contribute to further dislocating collisions. Also particles moving above the surface, i.e., sputtered atoms, are removed from the cascade.
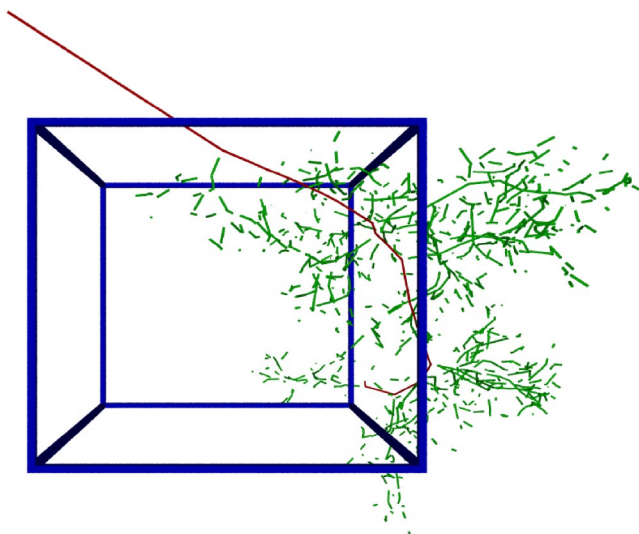

FIG. 1. Sample cascade originating from an impact of a 5 keV Cu ion on a Cu crystal. The angle of incidence is 60°. The cube shown acts just as scale and has size 2.65 nm^3, while the full lattice simulated has size $(10.6 \text{ nm})^2 \times 18$ nm.

Although this method has its limitations,[25] it has become a standard technique and is used to describe ion implantation and sputtering.

We have performed BCA simulations of single-ion impact on a flat Cu surface with velocity $\mathbf{v}_0$. Most of the time we consider normal incidence (i.e., $\mathbf{v}_0 = -|\mathbf{v}_0|\mathbf{e}_z$), but we also performed a few off-normal simulations to check for universal features, see below. A sample cascade, originating from an impact of a 5 keV Cu ion on a Cu lattice with an angle of incidence of 60°, is shown in Fig. 1. All the statistical information presented below was obtained from ensembles of 3000–6000 ion impacts per ensemble, which we generated for a single initial condition of the ion. We, moreover, considered two orientations of the crystal, (1,0,0) and $(58,72,\bar{3}9)$. The latter was used to assess the effects of crystal anisotropy and can be also considered as an alternative way to study changes with the angle of incidence. Most results which are of interest for comparison with the standard morphological theory and the ulterior analytic treatment are independent of the crystal orientation, as far as we can say. E.g., we found very good agreement between the angular averages of n_{2d}, ϵ_{2d} obtained from (1,0,0) and the corresponding quantities obtained from the oblique orientation. Hence, we believe that our results and conclusions for the surface morphology really represent generic features.

Our choices allowed for easy calibration and comparison of our implementation against results in the literature. It should be emphasized, however, that the main focus of the present work is on generic results, which are of relevance for pattern formation of ion-sputtered surfaces of metals.

IV. SIMULATION RESULTS

In this section we will present simulation results for the quantities introduced in Sec. II. As all quantities are evalu-
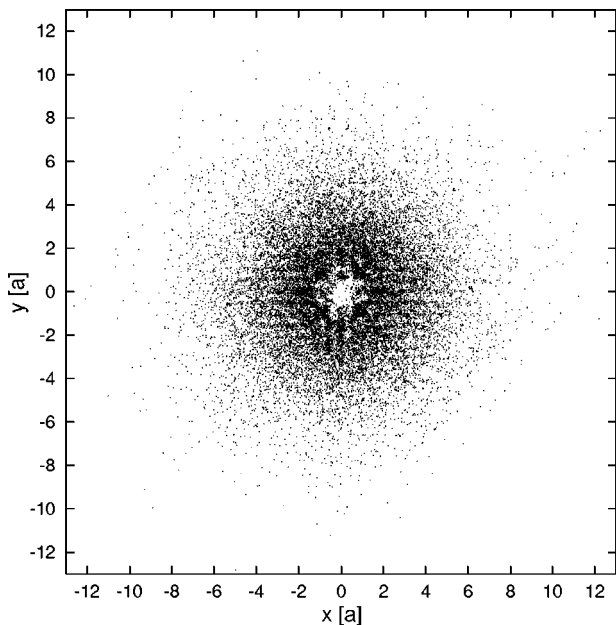
FIG. 2. Spatial distribution of ejected Cu atoms emerging from 6000 independent trials of hitting the (x, y) crystal surface [oriented in $(1,0,0)$ direction] with a single 5 keV Cu ion at normal incidence. Distances are measured in units of $a = 3.61$ Å.

ated at the surface $(z = 0)$, we will abbreviate the notation and drop the z coordinate from the list of variables whenever $z = 0$. So, for example, $n_{2d}(\boldsymbol{\rho}, z = 0) = n_{2d}(\boldsymbol{\rho})$.

Figure 2 shows the surface distribution of all the ejected particles within an ensemble of 6000 cascades, each emerging from one incident 5 keV Cu ion (normal incidence) for the crystal in the $(1,0,0)$ orientation. Clearly, a "hole" around the location of impact is visible. This is in contrast to what can be expected when applying Eq. (1). A similar effect in the ejection pattern, but at zero temperature, has already been seen for normal sputtering of 1 keV Ar$^+$ on Cu in the work by Yamamura and Takeuchi.[35] This hole can be explained by the facts that direct backscattering of the surface atoms is not possible, and that most collision cascades are directed away from the point of penetration, hence making it unlikely that surface atoms are ejected there. This is the main qualitative result of our simulations. Moreover, we also find this hole for off-normal incidence, as show in Fig. 3. Quantitatively, such origin for the hole can be assessed by studying correlations between the position $\boldsymbol{\rho}$ of sputtered particles and the projection of their velocities onto the surface, $\mathbf{v}_{surf} = \mathbf{v} - (\mathbf{v} \cdot \mathbf{e}_z)\mathbf{e}_z$. Figure 4 shows the distribution of the angle κ between $\boldsymbol{\rho}$ and $\mathbf{v}_{surf}$, where $\boldsymbol{\rho}$ is the position of a cascade particle arriving at the surface with velocity $\mathbf{v}$. The figure shows that, indeed, for typical collision cascades most of the ejected particles move away from the point of first ion impact.

The scattering of points in Fig. 2 is almost rotationally invariant; a slight square symmetric structure is visible, reflecting the lattice structure. Stronger anisotropies can be found at zero temperature[35] or when studying the movement of the particles inside collision cascades directly.[28–30] Here, we are interested mainly in the lateral ejection pattern of the sputtering. To check whether the result of finding a hole is an
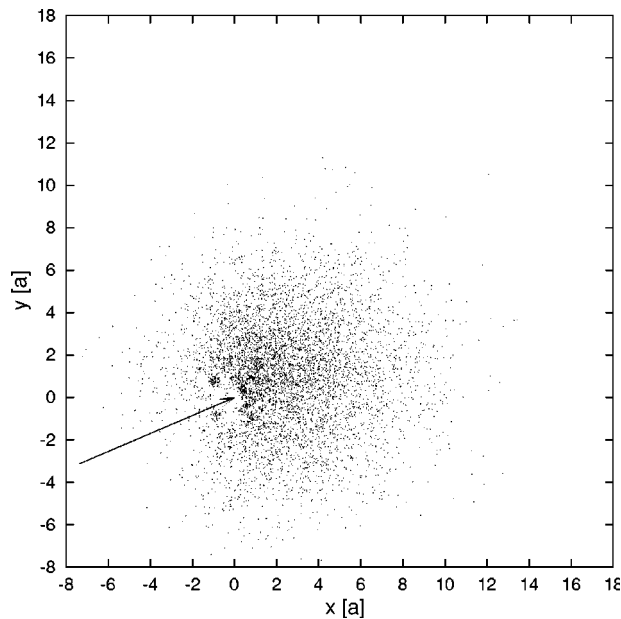

FIG. 3. Spatial distribution of ejected Cu atoms emerging from 6000 independent trials of hitting the (x, y) crystal surface [oriented in $(1,0,0)$ direction] with a single 5 keV Cu ion at 30° off-normal incidence. The arrow indicates the direction of the projection of the ion beam onto the surface. Distances are measured in units of $a = 3.61$ Å.

artifact of the crystal orientation, we studied also a $(58, 32, \bar{3}9)$ surface, see Fig. 5. Although the plot exhibits slightly less structures, again only a few particles are ejected near the point of penetration. It seems that the hole around this point is slightly smaller, as compared with Fig. 2. This is probably due to the lower symmetry of the crystal with re-
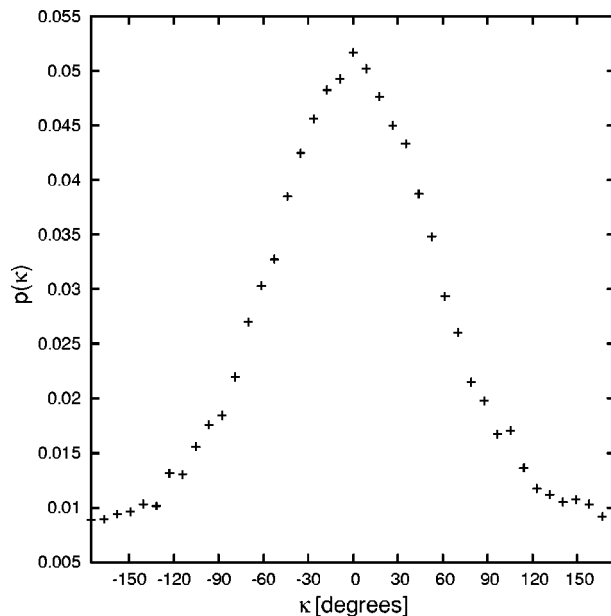

FIG. 4. Distribution of ejected particles with different directions of velocity. Here, κ denotes the angle between the projection of particle velocity onto the surface and the vector between point of ion impact and point of particle ejection.
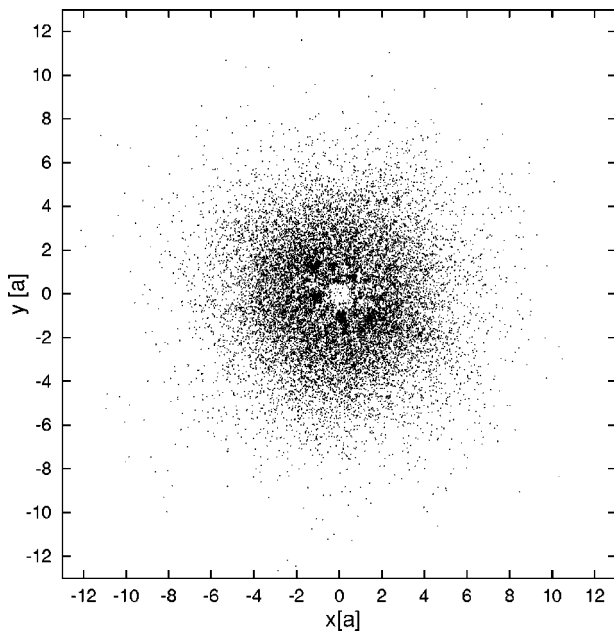
FIG. 5. Spatial distribution of ejected Cu atoms emerging from 6000 independent trials of hitting the (x,y) crystal surface [oriented in $(58,32,\bar{3}9)$ direction] with a single 5 keV Cu ion at normal incidence. Distances are measured in units of $a=3.61$ Å.

spect to the ion beam, which makes it more likely that collision cascades come back to the origin, i.e., the effect of focusing[29] is smaller. Hence, we decided to concentrate on the oblique $(58,32,\bar{3}9)$ orientation, because we want to study generic results irrespective of specific crystal orientations. In any case, for both surface orientations and small values of Δ, the angular average of the density introduced in Eq. (5) and defined by

$$n_{2d}(\rho) = \frac{1}{2\pi\rho\Delta}\int_0^{2\pi}d\phi\int_\rho^{\rho+\Delta}\rho'd\rho' n_{2d}(\rho',\phi), \qquad (8)$$

where $\rho=|\boldsymbol{\rho}|$, turns out to be nearly undistinguishable. Figure 6 shows the corresponding (angle-averaged) probability density per surface area [see Eq. (7)], $p(\rho) =1/(2\pi\rho\Delta)\int_0^{2\pi}d\phi\int_\rho^{\rho+\Delta}\rho'd\rho' p(\rho',\phi)$, of finding an ejected particle at a distance ρ from the point of incidence of the Cu ion. This figure shows that the assumption on the ejection probability being distributed following a Gaussian distribution, hence leading to a maximum at $\rho=0$, is not justified in the case of crystals. Hence, the question arises, whether this is in contrast to amorphous materials. Some studies[28,39,40] have been previously performed using Monte Carlo code such as TRIM to study sputtering in amorphous materials. Quantities like flux densities of particles/momentum, anisotropy parameters and densities of deposed energy/momentum were studied as a function of *depth*, and good agreement with the Sigmund theory was found. Nevertheless, to our knowledge there exists only one recent work,[41] in which, using the simulation packet SRIM, the ejection probability has been systematically studied *as a function of the lateral distance* from the point of penetration, and indeed a Gaussian-like distribution was observed for the same ion/bulk parameters as applied here.

Figure 7 displays the corresponding angular average of the surface density $\epsilon_{2d}(\rho)$ of the energy of sputtered particles, defined from Eq. (6) analogously to $n_{2d}(\rho)$ in Eq. (8). In this figure, we also show two Marquardt–Levenberg fits (for functions of the form $f_s=(a\rho^2+b\rho)\exp[-c\rho^s]$ with $s=1$ and $s=2$) to the data. One can see that the decay of the energy density is not in accordance with a Gaussian, even when including a decay towards the point of penetration, $\rho=0$, as suggested by Eq. (1). Rather, data can be fitted well to an exponential decay with a simple polynomial prefactor.
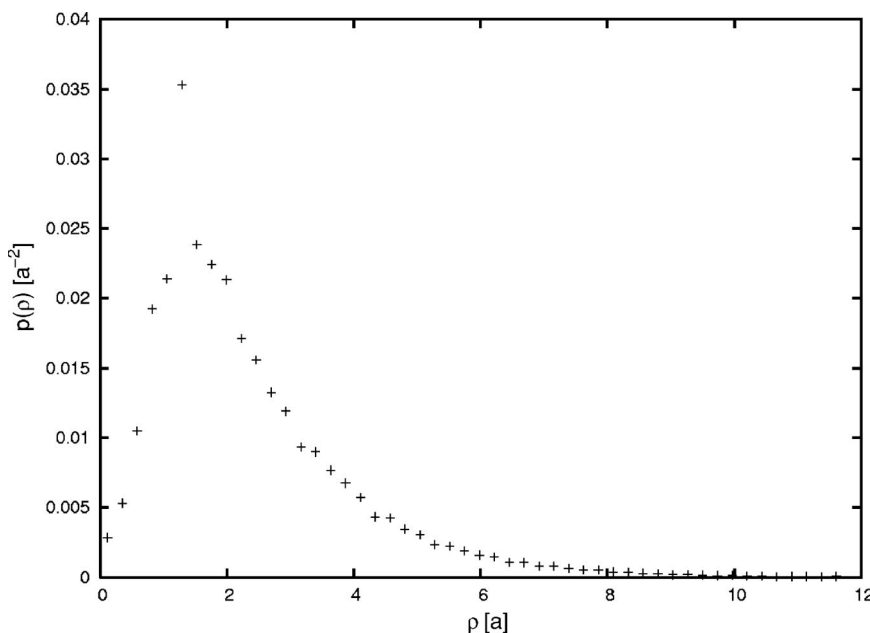

FIG. 6. Probability of ejected particles vs distance ρ from point of ion incidence (measured in units of $a=3.61$ Å), as determined from the data of Fig. 5.
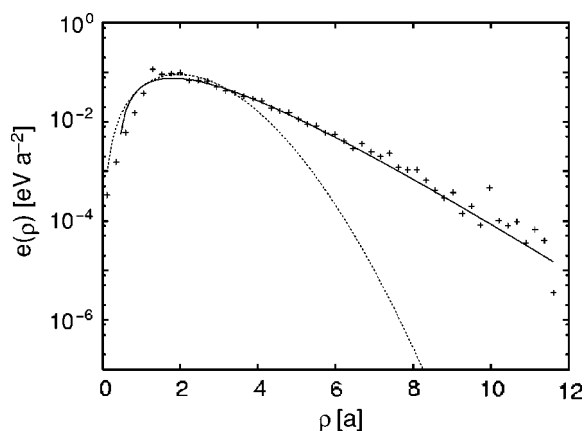
FIG. 7. Surface density of mean energy of sputtered Cu atoms vs distance ρ (measured in units of $a=3.61$ Å) from point of ion incidence for 5 keV Cu ions on semilog scale. The solid line is the best fit of the data to an exponential with a polynomial prefactor, namely, $0.297(\rho^2-0.392\rho)\exp(-1.27\rho)$. The dotted line, which corresponds to a fit to a Gaussian, is obviously inadequate.

In the previous figure, we have studied the mean [see Eqs. (6) and (7)]; let us now consider other characteristic features of the probability density $p(\rho,\epsilon)$. Thus, in Fig. 8 we show the surface-integrated probability density $p(\epsilon)=\int d^2\boldsymbol{\rho}\, p(\epsilon,\rho)$. The behavior is compatible with a simple power law for for large ϵ, namely,

$$p(\epsilon) \approx \frac{q}{(b+\epsilon)^\alpha} \sim \epsilon^{-2}, \qquad (9)$$

our best fit corresponding to $q=5.26$, $b=5.03$, $\alpha=1.87$. Figure 9 displays the conditional probability density $p(\epsilon|\rho)$ of
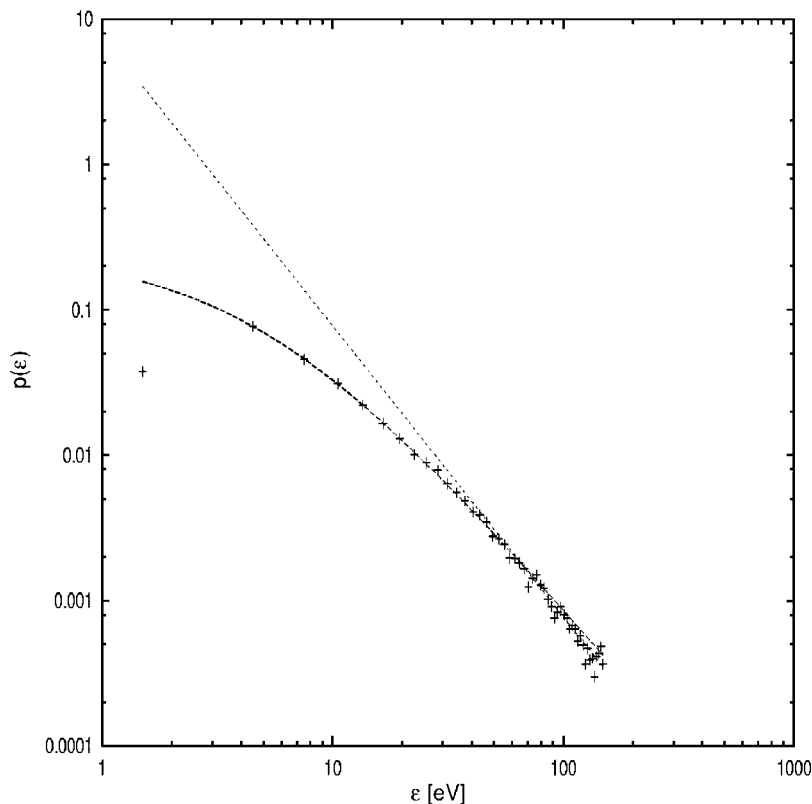
energy at fixed ρ, for different values of ρ. Remarkably, the conditional density does not depend on ρ significantly, within the statistical scatter, which is large for large energies. This shows that

$$p(\epsilon,\rho) \approx p(\rho)p(\epsilon) \sim \frac{n_{2d}(\rho)}{\epsilon^2} \qquad (10)$$

outside a region of very small distances. An immediate implication is that

$$\epsilon_{2d}(\rho) \propto n_{2d}(\rho), \qquad (11)$$

so that the number of ejected particles and the energy deposited at the surface are proportional to each other, as assumed in the BH theory. However, another important implication is that the amount of energy transported to the surface is subject to strong internal noise, as the number of ejected particles clearly is. This means that the energy flow varies strongly with time and space. Hence, fluctuations may play an important role for pattern formation. This may limit the applicability of deterministic continuum theories based on the average energy, which do not treat the fluctuations correctly. This problem will be pursued elsewhere.

V. CONTINUUM APPROXIMATION TO ENERGY DEPOSITION

Within Sigmund's approximation,[42] the rate at which the target is being eroded at an arbitrary point on the surface is proportional to the total amount of energy deposited there from ion collisions. In his theory for amorphous or polycrystalline targets, an accurate description of the sputtering phe-

FIG. 8. Probability density of energy, which is transported to the surface by a single collision cascade emerging from a 5 keV Cu ion, on a log-log scale. The solid line corresponds to the function $5.259(5.035+\epsilon)^{-1.874}$, which is the best fit to a simple power law $q/(b+\epsilon)^\alpha$, while the straight line represents a simple ϵ^{-2} power law.
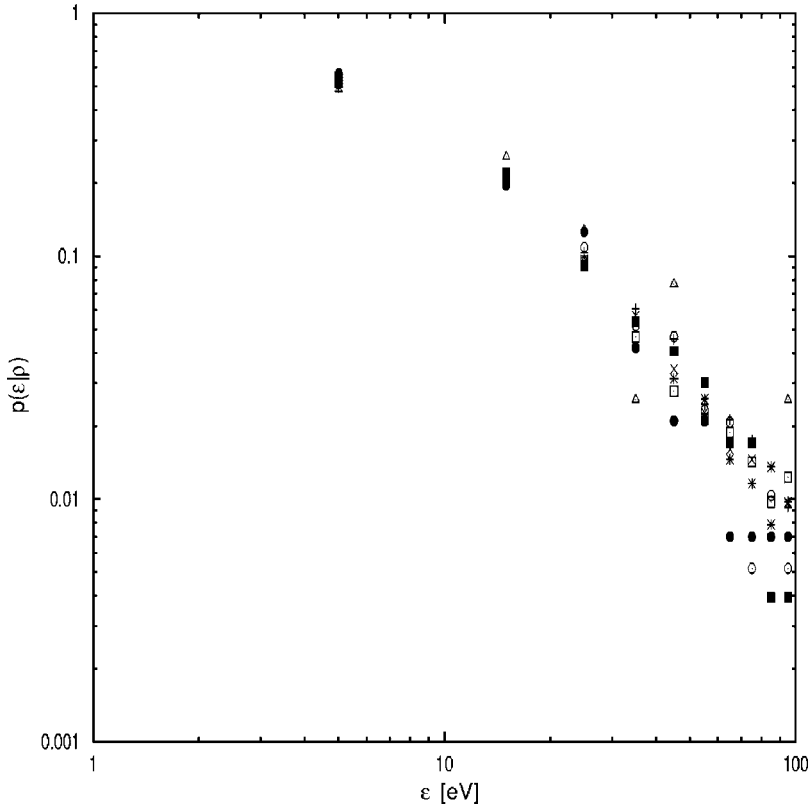
FIG. 9. Conditional probability density $p(\epsilon|\rho)$ to find energy ϵ for ejected particles keeping the distance ρ fixed. Different symbols correspond to different values $1.8 \leqslant \rho \leqslant 10.0$.

nomena can be achieved by assuming that energy is deposited following the Gaussian distribution (1).

Bradley and Harper[7] later employed this energy distribution in order to *compute* the *local* erosion velocity at an arbitrary surface point O, allowing for gentle surface undulations. To perform the calculation, a new local reference frame is taken in which the $\hat{\mathbf{z}}'$ axis is taken along the surface normal at O. The principal curvatures are assumed along the $\hat{\mathbf{x}}'$ and $\hat{\mathbf{y}}'$ axes that are defined, respectively, as the direction orthogonal to $\hat{\mathbf{z}}'$ that is in the plane defined by this axis and the ion trajectory and the remaining direction in order to make up a right-handed reference frame. Assuming that the radii of curvature at O, R_x, and R_y are much larger than the average penetration depth $\bar{a}$ the surface height can be approximated to $z'(x',y') = -\frac{1}{2}[(x'^2/R_x)+(y'^2/R_y)]$. In order to obtain the erosion velocity, we have to add up the total energy deposited at O from ions entering the whole target, expressing the ion flux and energy distribution in the latter reference frame, which is related with the one implicit in Eq. (1) as

$$\hat{\mathbf{x}} = \hat{\mathbf{x}}' \cos(\gamma_0) + \hat{\mathbf{z}}' \sin(\gamma_0),$$

$$\hat{\mathbf{y}} = \hat{\mathbf{y}}', \quad \hat{\mathbf{z}} = \hat{\mathbf{z}}' \cos(\gamma_0) - \hat{\mathbf{x}}' \sin(\gamma_0), \quad (12)$$

with γ_0 being the incidence angle formed between the ion trajectories and the *local* surface normal at O. Accounting up to curvature corrections, the ion flux reads $\Phi(x',y') = \Phi_0[\cos \gamma_0 - (x'/R_x)\sin \gamma_0]$, where Φ_0 is the *constant* nominal ion flux. Taking all this into account, the erosion velocity at O reads, finally,

$$v_O(\gamma_0, R_x, R_y) = \Lambda \int_{-\infty}^{+\infty} \int_{-\infty}^{+\infty} \Phi(x',y')\epsilon_{2d}(x',y')dx'\,dy',$$

$$(13)$$

where Λ is a proportionality constant relating deposited energy with the number of sputtered atoms, and the integration limits are taken to infinity thanks to the assumed fast decay of the energy distribution, taken by BH to be Sigmund's Gaussian, namely, $\epsilon_{2d} = \epsilon_s$ in Eq. (13). By expanding this equation to lowest nontrivial order in $\bar{a}/R_x$, $\bar{a}/R_y \ll 1$, Bradley and Harper obtained[7]

$$v_O = N_s \Lambda \epsilon \Phi_0 e^{-(\bar{a}^2/2\alpha^2)}\left[\Gamma_0(\gamma_0) + \frac{\Gamma_x(\gamma_0)}{R_x} + \frac{\Gamma_y(\gamma_0)}{R_y}\right],$$

$$(14)$$

where $\Gamma_0(\gamma_0)$, $\Gamma_x(\gamma_0)$, and $\Gamma_y(\gamma_0)$ are functions that depend not only on the incidence angle γ_0, but also on features of the energy distribution such as $\bar{a}$, α, and β.

A. Sputtering yield

Formula (14) enables computation of various relevant observables. Thus, the sputtering yield $Y(\gamma_0)$, defined as the total number of sputtered atoms per incident ion, is easily related to v_O by geometry as $Y(\gamma_0) = nv_O(\gamma_0)/(\Phi_0 \cos \gamma_0)$, where n is the number of atoms per unit volume in the target. Assuming a flat interface, that is, in the R_x, $R_y \rightarrow \infty$ limit, one is left with
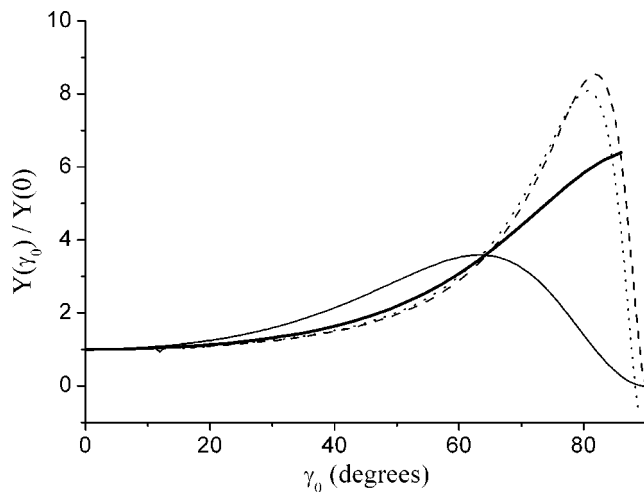
FIG. 10. Normalized sputtering yield $Y(\gamma_0)/Y(0)$ as a function of incidence angle γ_0, for the various one-dimensional energy distributions. Thick solid line: Bradley–Harper for $\bar{a}=3.8$ nm, $\alpha=2.2$ nm, $\beta=1.5$ nm. Thin solid line: modified Gaussian, Eq. (21), for $\bar{a}=3.8$ nm, $\sigma_z=2.2$ nm, $\sigma_x=1.5$ nm. Dashed line: exponential, Eq. (23), for $\bar{a}=3.8$ nm, $\sigma_z=2.2$ nm, $\sigma_x=0.28$ nm, $c=-0.14$ nm. Dotted line: truncated exponential, Eq. (23) with $c=0$ nm, and $\bar{a}=3.8$ nm, $\sigma_z=2.2$ nm, $\sigma_x=0.28$ nm.

FIG. 11. Normalized sputtering yield $Y(\gamma_0)/Y(0)$ as a function of incidence angle γ_0, for the various two-dimensional energy distributions. Thick solid line: Bradley–Harper for $\bar{a}=3.8$ nm, $\alpha=2.2$ nm, $\beta=1.5$ nm. Thin solid line: modified Gaussian, Eq. (20), for $\bar{a}=3.8$ nm, $\sigma_z=2.2$ nm, $\sigma_{xy}=1.5$ nm. Dashed line: exponential, Eq. (19), for $c=-0.14$ nm, $\bar{a}=3.8$ nm, $\sigma_z=2.2$ nm, $\sigma_{xy}=0.28$ nm. Dotted line: truncated exponential, Eq. (19) with $c=0$ nm, and $\bar{a}=3.8$ nm, $\sigma_z=2.2$ nm, $\sigma_{xy}=0.28$ nm.

$$Y(\gamma_0) = \frac{nv_O(\gamma_0, R_x \to \infty, R_y \to \infty)}{\Phi_0 \cos\gamma_0} \propto \frac{\Gamma_0(\gamma_0)}{\cos\gamma_0}. \quad (15)$$

Note that, for a flat surface, the local angle of incidence γ_0 coincides with the angle between the ion beam and the normal to the uneroded substrate. Working with Sigmund's distribution (1), BH found[7] that $Y(\gamma_0)$ increases monotonously as a function of γ_0—examples of the behavior of $Y(\gamma_0)$ as a function of γ_0 using BH's results are provided by the thick solid lines in Figs. 10 (for one-dimensional substrates) and 11 (for two-dimensional substrates)—such that the maximum efficiency for erosion is achieved at grazing incidence, contrary to experimental evidence for amorphous, polycrystalline, and crystalline targets.[43–45] This feature of the BH theory originates in a property of Sigmund's distribution, whose maximum for deposition, $\mathbf{r}=(0,0,-\bar{a})$, is located right at the surface under grazing incidence conditions. However, as is well known, there usually exists a value of $\gamma_0 < 90°$ for which the yield is maximum, such that the sputtering efficiency decreases for larger angles of incidence due to ions being reflected at the surface, an effect which is beyond Sigmund's approximations.

B. Surface morphology

Additional predictions on the morphology of the eroded target can be derived from Eq. (14). Thus, $\Gamma_x(\gamma_0)$ is negative[7] for small local angles of incidence, which implies that the erosion velocity is larger at troughs $(R_x < 0)$ than at peaks $(R_x > 0)$, inducing a morphological instability. Other surface relaxation mechanisms exist, such as surface diffusion, that counteract this instability. Competition between the two opposing phenomena induces the emergence of a typical length
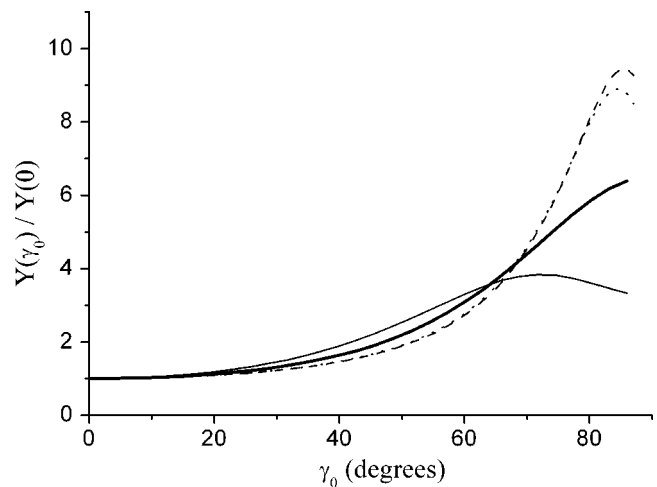
scale that provides the wavelength of the periodic ripple structure which appears. The best way to assess the features and properties of such a pattern is through the dynamical equation for the surface height derived by Bradley and Harper, which we briefly recall for the sake of the reader and for later reference. Thus, starting from the equation for the erosion velocity, consider now a laboratory frame of reference $(\hat{\mathbf{X}}, \hat{\mathbf{Y}}, \hat{\mathbf{Z}})$, defined as follows: the $\hat{\mathbf{Z}}$ axis is chosen to be normal to the initial flat surface. The incoming beam direction forms an angle θ with $\hat{\mathbf{Z}}$, and both direction define a plane where the $\hat{\mathbf{X}}$ axis lies. Finally, the $\hat{\mathbf{Y}}$ axis is perpendicular to the $\hat{\mathbf{X}}$ and $\hat{\mathbf{Z}}$ directions. We describe by $h(X,Y,t)$ the surface height at time t above point (X,Y) on the reference plane of the unbombarded substrate and assume that it varies slowly enough so that we can work to first order in the derivatives. In this way, we may approximate:[7–9] $\gamma_0 = \theta - \partial h/\partial X$, $(1/R_x) = -(\partial^2 h/\partial X^2)$, $(1/R_y) = -(\partial^2 h/\partial Y^2)$. Note that, for a flat interface, $\gamma_0 = \theta$. The velocity of erosion of the surface height h is provided by (minus) the erosion rate v_O, and we thus get

$$\frac{1}{F}\frac{\partial h}{\partial t} \cong -\Gamma_0(\theta) + \frac{\partial\Gamma_0(\theta)}{\partial\theta}\frac{\partial h}{\partial X} + \Gamma_x\frac{\partial^2 h}{\partial X^2} + \Gamma_y\frac{\partial^2 h}{\partial Y^2}, \quad (16)$$

where in our normalization F is a proportionality constant between v_O and Γ_0, Γ_x, Γ_y, which can be found in the Appendix for the various distributions considered of energy deposition. Considering a periodic perturbation to the flat surface $h(X,Y,t=0)=Ae^{i(k_1X+k_2Y)}$, and substituting this expression into Eq. (16), the surface profile evolves as

$$h(X,Y,t) = -\Gamma_0 t + Ae^{rt}e^{i(k_1X+k_2Y-\omega t)},$$

$$r = -\Gamma_x k_1^2 - \Gamma_y k_2^2, \quad \omega = -\Gamma_0' k_1. \quad (17)$$

If Γ_x and/or Γ_y are negative, there will be values for the wave vector (k_1, k_2) of the perturbation that make it grow exponentially. This behavior is the mathematical expression of the physical instability mentioned above, leading to ripple formation,[7,42] and is due to the curvature dependence of the erosion velocity that is larger in surface troughs than in surface protrusions. The observed ripple wavelength arises when additional smoothing mechanism such as surface diffusion exist that compete with the sputter instability, leading to selection of a specific length scale. Taking these mechanisms into account,[7–9] Eq. (16) reads

$$\frac{\partial h}{\partial t} \cong F\left\{ -\Gamma_0(\theta) + \frac{\partial \Gamma_0(\theta)}{\partial \theta} \frac{\partial h}{\partial X} + \Gamma_x \frac{\partial^2 h}{\partial X^2} + \Gamma_y \frac{\partial^2 h}{\partial Y^2} \right\} - B \nabla^4 h,$$

$$(18)$$

where, in principle, B is a thermally activated coefficient which depends on the surface self-diffusivity D_s, the free energy per unit area γ, and the number of atoms per unit area moving across the surface σ, as $B = 2D_s \gamma \sigma / (n^2 k_B T)$. In this case, $r = -\Gamma_x k_1^2 - \Gamma_y k_2^2 - B(k_1^2 + k_2^2)^2$, and there is only a band of unstable perturbations. The observed ripple wavelength λ is provided by the wave vector which has the largest *positive* value of r, and has a value $\lambda \propto [B/(F|\Gamma|)]^{1/2}$, with Γ being that coefficient, out of Γ_x and Γ_y, which, being negative, has the largest absolute value. Actually, working with Sigmund's distribution (1), BH obtained[7] that $\Gamma_x(\theta) \le \Gamma_y(\theta) < 0$ for incidence angles $0 \le \theta \le \theta_c$, whereas one has $\Gamma_y(\theta) < \Gamma_x(\theta)$ for $\theta > \theta_c$, with Γ_y being negative for all angles up to grazing incidence. Morphologically, this means that for small angles of incidence $0 \le \theta \le \theta_c$, ripple crests are oriented perpendicular to the $\hat{\mathbf{x}}'$ direction (the projection of the ion beam onto the substrate plane), whereas they are oriented perpendicular to the $\hat{\mathbf{y}}'$ direction for incidence angles larger than the critical one, θ_c. Many experiments[2,20,46] have verified the validity of the BH theory to describe ripple wavelength and orientation.

VI. MODIFIED ENERGY DISTRIBUTION FUNCTIONS

The results of computer simulations within the BCA approximation, obtained in the previous sections for Cu ion bombardment of a Cu target, are described by an energy distribution that differs substantially from that obtained by Sigmund in the case of polycrystalline or amorphous substrates. Using cylindrical coordinates around the ion trajectory, as in previous sections, we have (recall Fig. 7 above)

$$\epsilon_e(\boldsymbol{\rho}, z) = N_e \epsilon (\rho^2 + c\rho) e^{-(\rho/\sigma_{xy})} e^{-[(z+\bar{a})^2/2\sigma_z^2]}, \quad (19)$$

where $N_e = [(2\pi)^{3/2} \sigma_z (6\sigma_{xy}^4 + 2c\sigma_{xy}^2)]^{-1}$ is a normalization constant. Values for c and σ_{xy} that best fit simulation results were $c = -0.14$ nm, $\sigma_{xy} = 0.28$ nm, see Fig. 7. Note two main differences between distribution (19) and Sigmund's distribution (1): decay here is slower [exponential as compared to Gaussian, thus the subscripts in Eq. (19)] in the plane perpendicular to the ion trajectory, and energy deposition is *null* along the ion trajectory itself. On the other hand, distribution (19) is unphysical since $c < 0$ leads to *negative* probabilities

for small ρ values. Nevertheless, as we will see, qualitative *morphological results* do not vary much if we consider, e.g., a "truncated exponential" distribution (19) with $c = 0$, which is, now, physical, and preserves both main features of Eq. (19), namely, zero energy deposition along the ion trajectory and exponential decay. However, as a difference with BH results, *for any value of c, Eq. (19) is not amenable (in the case of two-dimensional substrates, see below) to analytical results for the coefficients appearing in the erosion velocity as a function of experimental parameters. For this reason, and in order to facilitate analytical results in such cases, we will also consider the following modified Gaussian (thus the subscripts) distribution*:

$$\epsilon_g(\boldsymbol{\rho}, z) = N_g \epsilon \rho^2 e^{-[\rho^2/(2\sigma_{xy}^2)]} e^{-[(z+\bar{a})^2/2\sigma_z^2]},$$

$$N_g = [2(2\pi)^{3/2} \sigma_{xy}^4 \sigma_z]^{-1}, \quad (20)$$

which, again, shares with Eq. (19) inducing zero energy deposition along the ion trajectory $\rho = 0$, but is otherwise Gaussian in all three directions far enough from the ion path.

A. One-dimensional interfaces: Sputtering yields

In order to develop intuition about morphological predictions from Eqs. (19) and (20), we consider first the (nonphysical) case of a one-dimensional target, whose surface height is described by a single variable function $z'(x')$, or $h(X)$. These results will be then compared to the analogous ones by Bradley and Harper, which will allow us to assess differences due to the new form of the energy distribution—mostly due to the fact that in our case no energy is deposited along ion trajectories.

For a one-dimensional target, distribution (20) reads

$$\epsilon_g^{1d}(x, z) = N_g \epsilon x^2 e^{-[x^2/(2\sigma_x^2)]} e^{-[(z+\bar{a})^2/2\sigma_z^2]},$$

$$N_g^{1d} = (2\pi \sigma_z \sigma_x^3)^{-1}. \quad (21)$$

Writing the local velocity of erosion in terms of $\Gamma_0^{g,1d}$, $\Gamma_x^{g,1d}$ analogous of those in Eq. (14), we obtain

$$v_O = N_g^{1d} \Lambda \epsilon \Phi_0 e^{-[\bar{a}^2/(2\sigma_z^2)]} \left[\Gamma_0^{g,1d} + \frac{\Gamma_x^{g,1d}}{R_x} \right], \quad (22)$$

where the full expressions for $\Gamma_0^{g,1d}$ and $\Gamma_x^{g,1d}$ as functions of γ_0, $\bar{a}$, σ_x, and σ_z can be found in Appendix A 1.

On the other hand, distribution (19) reads, for a one-dimensional interface,

$$\epsilon_e^{1d}(x, z) = N_e \epsilon (x^2 + c|x|) e^{-(|x|/\sigma_x)} e^{-[(z+\bar{a})^2/2\sigma_z^2]},$$

$$N_e^{1d} = [\sqrt{2\pi} \sigma_z (4\sigma_x^3 + 2c\sigma_x^2)]^{-1}. \quad (23)$$

In this case, the prediction for the local velocity of erosion has a shape that is similar to Eq. (21), albeit with more complex coefficients, whose detailed analytical expressions are again left to Appendix A 2:

$$v_O = N_e^{1d} \Lambda \epsilon \Phi_0 e^{-[\bar{a}^2/(2\sigma_z^2)]} \left[\Gamma_0^{e,1d} + \frac{\Gamma_x^{e,1d}}{R_x} \right]. \qquad (24)$$

In Fig. 10, we plot the normalized (to the corresponding values for normal incidence) sputtering yields $Y(\gamma_0)$ obtained through formula (15) for the modified Gaussian (21) and exponential (23) distributions. For the sake of reference, the BH yield is also shown (thick solid line). Parameters employed in Fig. 10 are typical for Cu ion bombardment of Cu for energies in the range of a few keV, as confirmed by TRIM/SRIM simulations.[21] We can see that for both modified distributions, Eqs. (21) and (23), the corresponding yields feature maxima before grazing incidence, as a difference to the BH curve. This is in agreement with experimental data,[43–45] and is due to the fact that maxima of energy deposition are not along the ion trajectory for these distributions but, rather, at a certain finite distance from it, which makes grazing incidence *not* the most efficient one for sputtering. From the figure, we can also conclude that changing the value of parameter c in distribution (23) from the value deduced from the BCA simulations (dashed line) to $c=0$ ("truncated exponential distribution," dotted line) does not modify greatly the quantitative behavior. A larger quantitative modification [but not qualitative, in the sense that, in all cases, $Y(\gamma_0)$ is maximum for nongrazing incidence] is obtained when decay is Gaussian [distribution (21), thin solid line in the figure], rather than exponential.

The fact (seen in Fig. 10) that the yield is negative for large incidence angles γ_0, as computed using the exponential distribution with $c<0$, is due to Eq. (23) taking negative values for small distances to the ion path. As will be seen below, this is an artifact of the one-dimensional approximation, as is the fact that the yields computed from the modified Gaussian distribution (21), and from the exponential distribution (23) with $c=0$, vanish for $\gamma_0=90°$.

B. Two-dimensional interfaces

Naturally, the physically relevant case is bombardment of two-dimensional targets. In this case, the analysis is more complex, to the extreme that no closed analytic expressions are available analogous of those found previously, for the exponential distribution (19) that best fits our BCA simulation data. Results for this distribution will be provided from numerical solutions of Eq. (13) using Eq. (19). On the other hand, we have seen in the 1d case that distributions (21) and (23) lead to similar qualitative results for the shape of the sputtering yield. For the 2d case, expression (13) using the modified Gaussian distribution (20) does lead to closed analytical expressions for the coefficients in

$$v_O = N_g \Lambda \epsilon \Phi_0 e^{-(\bar{a}^2/2\sigma_z^2)} \left[\Gamma_0^g + \frac{\Gamma_x^g}{R_x} + \frac{\Gamma_y^g}{R_y} \right], \qquad (25)$$

that can be found in Appendix A 3.

1. Sputtering yield

In Fig. 11 we see again that the sputtering yields for both modified distributions (19) and (20) have maxima for inci-

dence angles smaller than grazing, in contrast with the BH result (thick solid line), that is maximum only for $\gamma_0=90°$. As in the one-dimensional case, there is only a slight quantitative change in the yield curve if we change parameter c in the exponential distribution (19) from the value fitting BCA data (dashed line) to the truncated exponential value $c=0$ (dotted line). Also as in the 1d case, the quantitative change is larger if we consider, rather, the modified Gaussian distribution (20), the maximum of the yield being attained for smaller incidence angles. Note, incidentally, that maxima of the sputtering yield for Xe$^+$ bombardment of Cu have been reported to occur at *large but nongrazing* angles.[45] As in the 1d case, yield maxima at nongrazing angles are due to energy deposition being most efficient at a certain finite distance from the ion trajectory.

The yields displayed in Fig. 11 are positive and nonzero for all values of γ_0, and amount to large sputtering rates, as found in experiments.[43–45] In the present two-dimensional case, for grazing incidence the radial component of the energy distribution vanishes at the point of impact with the surface, but not at finite distances from it, which implies that after surface integration the total deposited energy is nonzero and the yield is positive.

2. Surface morphology

We are now in a position to study the consequences for the ripple formation process, of the new features presented—as compared with Sigmund's formula (1)—by the energy distribution (19), suggested by our BCA data, or its analytically more suited counterpart, Eq. (20). In order to do this, we follow the approach pioneered by Bradley and Harper. Once we take the assumption that the erosion velocity at a surface point is proportional to the total amount of deposited energy, and by incorporating surface diffusion effects, the steps sketched in Sec. V B lead us to an equation of the same form as Eq. (18), but with coefficients Γ_0, Γ_x, and Γ_y, that differ for each energy distribution function considered. As a partial consistency check of our results, note that for normal incidence, the $x \leftrightarrow y$ symmetry is restored on the substrate plane so that $\Gamma_x(0)$ and $\Gamma_y(0)$ must coincide. While for the case of Eq. (25), we obtain *analytically* $\Gamma_x^g(0) = \Gamma_y^g(0) = -4\pi\bar{a}\sigma_{xy}^6/\sigma_z^2$, for distribution (19) the equality has to be checked numerically, which indeed we have done.

In Figs. 12–14 we present results for the "effective surface tension" coefficients Γ_x and Γ_y for the various two-dimensional distributions that are normalized by their corresponding absolute values for normal incidence $\theta=0$ [note that in the interface equation, Eq. (18), the coefficients $\Gamma_{0,x,y}$ appear evaluated at value θ of their arguments]. We see in Figs. 13 and 14 that Γ_x is smaller than Γ_y for incidence angles $\theta < \theta_c$, and that Γ_y is always negative, similarly to the BH case, displayed for the reader's convenience in Fig. 12. One of the successes of BH's theory lies in its description of the orientation of the ripple structure for different ion incidence angles θ. Here we see that, although distributions (19) and (20) lead to quite different sputtering yields as compared to Sigmund's distribution, the qualitative behavior of coefficients Γ_x and Γ_y is quite similar to that found by BH, and thus leads to analogous morphological properties as de-
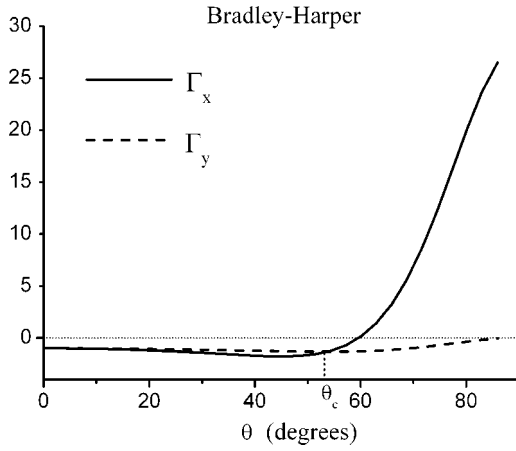
FIG. 12. Normalized values of Γ_x and Γ_y for the distribution (1) using the same parameter values as in Fig. 11.

scribed in Sec. V B. Moreover, since dependencies of the ripple wavelength $\lambda \propto \sqrt{B/(F|\Gamma|)}$ on parameters such as ion flux Φ_0, temperature, or average ion energy ϵ are due to those in the constants F and B, and these *are the same as those in BH* (see Appendix), Eq. (18) predicts these for Cu to be (qualitatively) the same as obtained from BH theory.[9] Note this is *also* the case in the presence of nonthermal surface diffusion in which, similarly to BH,[9] the constant B has no dependence on temperature and is rather proportional to F. Overall, given that experimental results are in good agreement with BH predictions for metals,[3,4,20] we can conclude that, in order to provide qualitative *analytical* estimates for morphological properties of ripple formation on metals, the modified Gaussian distribution (20) seems to be a reasonable choice.

VII. SUMMARY AND OUTLOOK

We have studied numerically the sputtering process of Cu ions on Cu fcc crystals by means of the binary-collision approximation. We have analyzed the distribution of sputtered particles and their energies, and found significant deviations from Sigmund's formula, which is traditionally employed to
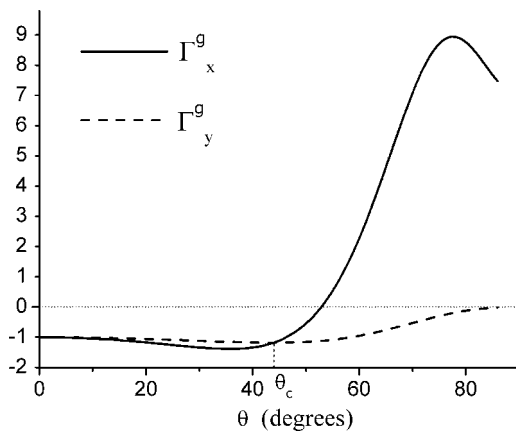

FIG. 13. Normalized values of Γ_x^g and Γ_y^g for the distribution (20) using the same parameter values as in Fig. 11.
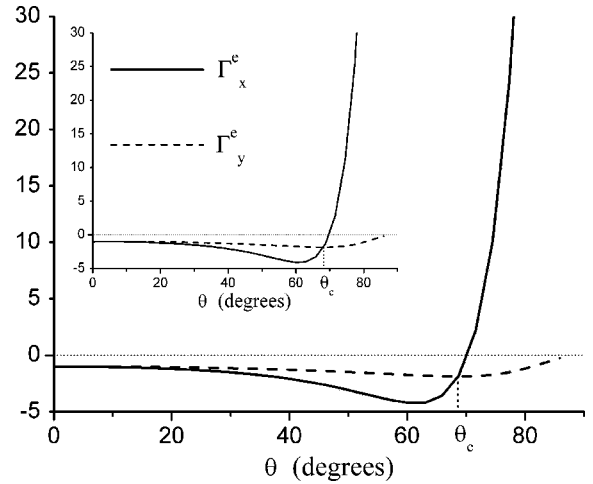

FIG. 14. Normalized values of Γ_x^e and Γ_y^e for the distribution (19) using the same parameter values as in Fig. 11. The inset corresponds to $c=-0.14$, while the main panel corresponds to $c=0$.

study the sputtering process in the framework of continuum theories, as applied to amorphous and polycrystalline substrates. In particular, we find that near the point where the ion penetrates the target, the sputter probability goes to zero, while the Bradley–Harper/Sigmund theory predicts maximum sputtering at that point.

We have fitted heuristic functions to our data. We find that an *exponential* (rather than *Gaussian* as in Sigmund's theory) decay with a combination of a quadratic and a linear prefactor fits the data well. The main physical effect, namely, the hole near the point of penetration, can be reproduced also qualitatively using a Gaussian distribution with a quadratic prefactor that lends itself to exact results. We have performed analytical calculations of the local erosion velocity following the Bradley–Harper approach for one- and two-dimensional surfaces for both types of modified distributions (for the two-dimensional exponential distribution, the equation could be solved only numerically). We find that the sputter yield is qualitatively different as compared with the BH approach. As a function of the angle of incidence, the yield exhibits a maximum at an angle smaller than 90°. This is in good agreement with experimental findings, in marked contrast with the analogous BH result using Sigmund's distribution, even without implementing explicitly reflection of the ions for grazing incidence, which is usually regarded as the main cause for the decay of the yield at grazing incidence. Finally, we have computed also the ripple orientation-determining parameters Γ_x and Γ_y, usually referred to in this context as effective surface tension parameters. These turn out to be only slightly modified with respect to the BH theory, and lead to a qualitatively similar pattern formation process. Dependencies of the ripple wavelength on phenomenological parameters, such as ion flux, ion average energy, and temperature are as in BH theory.[9] Since the influence of nonlinearities on ripple characteristics is still under debate even within Sigmund's theory proper, we have not considered this type of effects here. At any rate, the same type of nonlinear terms would appear in the interface Eq. (18) as compared to the corresponding equation for amorphous or polycrystalline substrates.[8,9]

Thus, as a general conclusion on pattern formation by ion-beam sputtering, our results justify the similarities found in experiments on metals, to the analogous processes in amorphous or amorphizable materials, and point to potential quantitative differences that would possibly merit further studies. Additional features of ripple formation in metals such as their existence for normal incidence or change of orientation with temperature[3,15,16] are *not* explained by the special properties of the collision cascades in these systems that we have studied here but, rather, by the special properties of surface diffusion in such anisotropic substrates.

Regarding future work, it would be also interesting to see whether the hole near the point of penetration can be found in experiments and/or in more detailed simulations (such as, e.g., by molecular dynamics). To our knowledge, no analysis of single-ion impacts on metals exist so far. Furthermore, it would be worth incorporating the modified energy distribution into existing simple Monte Carlo models of surface sputtering, such as those in Refs. 17 and 47, in order to improve their description of erosion processes in metallic substrates, specially at the large distance and long-time regime for which this type of models is particularly suited.

APPENDIX A: ANALYTIC EXPRESSIONS FOR COEFFICIENTS IN THE EROSION VELOCITY

In this appendix, we provide the full expressions for the coefficients appearing in various expressions for the surface erosion velocity, Eqs. (24), (22), and (25), that have been computed analytically for those energy distributions for which such type of results are achievable.

1. One-dimensional modified Gaussian distribution

$$v_O = F_g^{1d}\left[\Gamma_0^{g,1d} + \frac{\Gamma_x^{g,1d}}{R_x}\right],$$

$$F_g^{1d} = N_g^{1d}\Lambda\epsilon\Phi_0 e^{-[\bar{a}^2/(2\sigma_z^2)]},$$

$$\Gamma_0^{g,1d} = \frac{\sqrt{\pi}e^{A_g^2/(4B_g)}(A_g^2 + 2B_g)}{4B_g^{5/2}}\cos^3\gamma_0,$$

$$\Gamma_x^{g,1d} = \frac{\sqrt{\pi}e^{A_g^2/(4B_g)}}{32B_g^{11/2}}[2A_g^3 B_g(A_g b_g - 10c_g) - A_g^5 c_g$$
$$- 4A_g B_g^2(A^2 a_g - 6A_g b_g + 15c_g) - 24B_g^3(A_g a_g - b_g)],$$

$$A_g = \frac{\bar{a}}{\sigma_z^2}\sin\gamma_0, \quad B_g = \frac{1}{2\sigma_z^2}\sin^2\gamma_0 + \frac{1}{2\sigma_x^2}\cos^2\gamma_0,$$

$$a_g = -2\sin\gamma_0\cos^2\gamma_0, \quad b_g = -\frac{\bar{a}}{2\sigma_z^2}\cos^4\gamma_0,$$

$$c_g = \left(\frac{1}{2\sigma_x^2} - \frac{1}{2\sigma_z^2}\right)\cos^4\gamma_0\sin\gamma_0.$$

2. One-dimensional exponential distribution

$$v_O = F_e^{1d}\left[\Gamma_0^{e,1d} + \frac{\Gamma_x^{e,1d}}{R_x}\right],$$

$$F_e^{1d} = N_e^{1d}\Lambda\epsilon\Phi_0 e^{-[\bar{a}^2/(2\sigma_z^2)]},$$

$$\Gamma_0^{e,1d} = \frac{a_e}{B_e} + \frac{1}{8B_e^{5/2}}\sum_{i=1,2}\left\{-2\sqrt{B_e}A_{e,i}b_e + [A_{e,i}^2 b_e - 2a_e A_{e,i}B_e\right.$$
$$\left. + 2b_e B_e]\sqrt{\pi}e^{(A_{e,i}^2)/4B_e}\,\text{erfc}\left(\frac{A_{e,i}}{2\sqrt{B_e}}\right)\right\},$$

$$\Gamma_x^{e,1d} = \frac{1}{64B_e^{11/2}}\sum_{i=1,2}\left\{2\sqrt{B_e}((-1)^i A_{e,i}^4 f_e - 2A_{e,i}^3 B_e e_{e,i} + (-1)^i\right.$$
$$\times 16B_e^3 d_{e,i} - 4B_e^2\{A_{e,i}[5e_{e,i} + (-1)^i 2B_e c_e]\} + (-1)^i$$
$$\times 18A_{e,i}^2 B_e f_e + (-1)^i 4A_{e,i}B_e^2 d_{e,i}) + \{-(-1)^i A_{e,i}^5 f_e$$
$$+ 2A_{e,i}^3 B_e[A_{e,i}e_{e,i} - (-1)^i 10f_e] - 4A_{e,i}B_e^2[(-i)^i A_{e,i}^2 d_{e,i}$$
$$- 6A_{e,i}e_{e,i} + (-1)^i 15f_e] + 8B_e^3[(-1)^i A_{e,i}^2 c_e - (-1)^i$$
$$\left.\times 3A_{e,i}d_{e,i} + 3e_{e,i}]\}\sqrt{\pi}e^{A_{e,i}^2/(4B_e)}\,\text{erfc}\left(\frac{A_{e,i}}{2\sqrt{B_e}}\right)\right\},$$

$$A_{e,1} = \frac{\cos\gamma_0}{\sigma_x} - \frac{\bar{a}\sin\gamma_0}{\sigma_z^2}, \quad A_{e,2} = \frac{\cos\gamma_0}{\sigma_x} + \frac{\bar{a}\sin\gamma_0}{\sigma_z^2},$$

$$B_e = \frac{\sin^2\gamma_0}{2\sigma_s^2}, \quad a_e = c\cos^2\gamma_0, \quad b_e = \cos^3\gamma_0,$$

$$c_e = -\frac{3}{2}c\cos\gamma_0\sin\gamma_0,$$

$$d_{e,1} = \left(\frac{c}{2\sigma_x} - 2\right)\cos^2\gamma_0\sin\gamma_0 + \frac{c\bar{a}}{2\sigma_z^2}\cos^3\gamma_0,$$

$$d_{e,2} = \left(\frac{c}{2\sigma_x} - 2\right)\cos^2\gamma_0\sin\gamma_0 - \frac{c\bar{a}}{2\sigma_z^2}\cos^3\gamma_0,$$

$$e_{e,1} = \left(\frac{c}{2\sigma_z^2} - \frac{1}{2\sigma_x}\right)\cos^3\gamma_0\sin\gamma_0 - \frac{\bar{a}}{2\sigma_z^2}\cos^4\gamma_0,$$

$$e_{e,2} = -\left(\frac{c}{2\sigma_z^2} + \frac{1}{2\sigma_x}\right)\cos^3\gamma_0\sin\gamma_0 - \frac{\bar{a}}{2\sigma_z^2}\cos^4\gamma_0,$$

$$f_e = 2 \cos^5 \gamma_0 \sin \gamma_0.$$

3. Two-dimensional modified Gaussian distribution

$$v_O = F_g \left[\Gamma_0^g + \frac{\Gamma_x^g}{R_x} + \frac{\Gamma_y^g}{R_y} \right],$$

$$F_g = N_g \Lambda \epsilon \Phi_0 e^{-[\bar{a}^2/(2\sigma_z^2)]},$$

$$\Gamma_0^g = \frac{\pi e^{A_g^2/(4B_g)} (b_0 A_g^2 + 4 a_0 B_g^2 + 2 b_0 B_g)}{2\sqrt{2} B_g^{5/2}},$$

$$\Gamma_x^g = \frac{\pi e^{A_g^2/(4B_g)}}{16\sqrt{2} B_g^{11/2}} \{ 2B_g [4B_g^2 b_x (A_g^2 + 2B_g) - 8 A_g B_g^3 a_x$$
$$- 2 A_g B_g c_x (A_g^2 + 6B_g) + d_x (A_g^4 + 12 A_g^2 B_g + 12 B_g^2)]$$
$$- A_g e_x (A_g^4 + 20 A_g^2 B_g + 60 B_g^2) \},$$

$$\Gamma_y^g = \frac{\pi e^{A_g^2/(4B_g)}}{4\sqrt{2} B_g^{7/2}} [2 B_g c_y (A_g^2 + 2B_g) - 4 B_g^2 a_y (b_y - 2B_g)$$
$$- A_g d_y (A_g^2 + 6B_g)],$$

$$A_g = \frac{\bar{a}}{\sigma_z^2} \sin \gamma_0, \quad B_g = \frac{1}{2\sigma_z^2} \sin^2 \gamma_0 + \frac{1}{2\sigma_{xy}^2} \cos^2 \gamma_0,$$

$$a_0 = \sigma_{xy}^3 \cos \gamma_0, \quad b_0 = \sigma_{xy} \cos^3 \gamma_0,$$

$$a_x = -\sigma_{xy}^3 \sin \gamma_0, \quad b_x = -\frac{\sigma_{xy}^3}{2\sigma_z^2} \bar{a} \cos^2 \gamma_0,$$

$$c_x = -\left(\frac{3}{2} \sigma_{xy} + \frac{\sigma_{xy}^3}{2\sigma_z^2} \right) \cos^2 \gamma_0 \sin \gamma_0,$$

$$d_x = -\frac{\sigma_{xy}}{2\sigma_z^2} \bar{a} \cos^4 \gamma_0, \quad e_x = \left(\frac{1}{2\sigma_{xy}} - \frac{\sigma_{xy}}{2\sigma_z^2} \right) \sin \gamma_0 \cos^4 \gamma_0,$$

$$a_y = -\frac{3\sigma_{xy}^5}{2\sigma_z^2} \bar{a} \cos^2 \gamma_0,$$

$$b_y = -\frac{3\sigma_{xy}^5}{2\sigma_z^2} \cos^2 \gamma_0 \sin \gamma_0 + \frac{\sigma_{xy}^3}{2} \cos^2 \gamma_0 \sin \gamma_0,$$

$$c_y = -\frac{\sigma_{xy}^3}{2\sigma_z^2} \bar{a} \cos^4 \gamma_0, \quad d_y = \left(\frac{\sigma_{xy}}{2} - \frac{\sigma_{xy}^3}{2\sigma_z^2} \right) \cos^4 \gamma_0 \sin \gamma_0.$$

*Electronic address: hartmann@theorie.physik.uni-goettingen.de

†Electronic address: reiner.kree@physik.uni-goettingen.de

‡Electronic address: jamunoz@math.uc3m.es

§Electronic address: cuerno@math.uc3m.es

[1] G. W. Lewis, M. J. Nobes, G. Carter, and J. L. Whitton, Nucl. Instrum. Methods **179**, 363 (1980).

[2] E. Chason, T. M. Mayer, B. K. Kellermann, D. E. McIlroy, and A. J. Howard, Phys. Rev. Lett. **72**, 3040 (1994).

[3] S. Rusponi, G. Constantini, C. Boragno, and U. Valbusa, Phys. Rev. Lett. **81**, 4184 (1998).

[4] S. Habenicht, W. Bolse, K. P. Lieb, K. Reimann, and U. Geyer, Phys. Rev. B **60**, R2200 (1999).

[5] T. M. Mayer, E. Chason, and A. J. Howard, J. Appl. Phys. **76**, 1633 (1994).

[6] U. Valbusa, C. Boragno, and F. B. de Mongeot, J. Phys.: Condens. Matter **14**, 8153 (2002).

[7] R. M. Bradley and J. M. E. Harper, J. Vac. Sci. Technol. A **6**, 2390 (1988).

[8] R. Cuerno and A. L. Barabási, Phys. Rev. Lett. **74**, 4746 (1995).

[9] M. Makeev, R. Cuerno, and A. L. Barabási, Nucl. Instrum. Methods Phys. Res. B **197**, 185 (2002).

[10] C. M. Demanet, J. B. Malherbe, N. G. Vanderberg, and V. Sankar, Surf. Interface Anal. **23**, 433 (1995).

[11] S. W. MacLaren, J. E. Baker, N. L. Finnegan, and C. M. Loxton, J. Vac. Sci. Technol. A **10**, 468 (1992).

[12] G. Carter and V. Vishnyakov, Phys. Rev. B **54**, 17 647 (1996).

[13] J. Malherbe, CRC Crit. Rev. Solid State Mater. Sci. **19**, 55 (1994), and references therein.

[14] J. Erlebacher, A. J. Aziz, E. Chason, M. B. Sinclair, and J. A. Floro, Phys. Rev. Lett. **82**, 2330 (1999).

[15] S. Rusponi, C. Boragno, and U. Valbusa, Phys. Rev. Lett. **78**, 2795 (1997).

[16] S. Rusponi, G. Constantini, C. Boragno, and U. Valbusa, Phys. Rev. Lett. **81**, 2735 (1998).

[17] A. K. Hartmann, R. Kree, U. Geyer, and M. Kölbel, Phys. Rev. B **65**, 193403 (2002).

[18] E. O. Yewande, A. K. Hartmann, and R. Kree, Phys. Rev. B (to be published).

[19] P. Sigmund, Phys. Rev. **184**, 383 (1969).

[20] W. L. Chan, N. Pavenayotin, and E. Chason, Phys. Rev. B **69**, 245413 (2004).

[21] J. F. Ziegler, J. P. Biersack, and U. Littmark, *The Stopping and Range of Ions in Matter* (Pergamon, New York, 1985).

[22] T. A. Tombrello, Nucl. Instrum. Methods Phys. Res. B **83**, 508 (1993).

[23] M. T. Robinson and I. M. Torrens, Phys. Rev. B **9**, 5008 (1974).

[24] I. Koponen, M. Hautala, and O. P. Sievänen, Phys. Rev. Lett. **78**, 2612 (1997).

[25] M. T. Robinson, Radiat. Eff. Defects Solids **130**, 3 (1994).

[26] I. Koponen, M. Hautala, and O. P. Sievänen, Phys. Rev. B **54**, 13 502 (1996).

[27] V. Shulga, Radiat. Eff. **85**, 1 (1985).

[28] H. Whitlow and M. Hautala, Nucl. Instrum. Methods Phys. Res. B **18**, 370 (1987).

[29] M. Hautala and J. Likonen, Phys. Rev. B **41**, 1759 (1990).

[30] J. Likonen and M. Hautala, Phys. Rev. B **42**, 3838 (1990).

[31] R. Silsbee, J. Appl. Phys. **28**, 1246 (1957).

[32] V. Shulga, Radiat. Eff. **82**, 169 (1984).

[33] M. Hou and W. Eckstein, Nucl. Instrum. Methods Phys. Res. B **13**, 324 (1986).

[34] W. Eckstein and M. Hou, Nucl. Instrum. Methods Phys. Res. B **31**, 386 (1988).

[35] Y. Yamamura and W. Takeuchi, Nucl. Instrum. Methods Phys. Res. B **29**, 461 (1987).

[36] We performed also some test simulations for Ar ions and obtained qualitatively the same results. Hence, we show only the results for Cu ions here.

[37] G. Moliere, Z. Naturforsch. A **2**, 133 (1947).

[38] O. B. Firsov, Sov. Phys. JETP **36**, 1076 (1959).

[39] M. Hautala and H. Whitlow, Nucl. Instrum. Methods Phys. Res. B **6**, 466 (1985).

[40] M. Posselt, Nucl. Instrum. Methods Phys. Res. B **36**, 420 (1989).

[41] H. C. Hofsaess, (private communication).

[42] P. Sigmund, J. Mater. Sci. **8**, 1545 (1973).

[43] H. Oechsner, Appl. Phys. **8**, 185 (1975).

[44] K. B. Cheney and E. T. Pitkin, J. Appl. Phys. **36**, 3542 (1965).

[45] A. Olivia-Florio, R. A. Baragiola, M. M. Jakas, E. V. Alonso, and J. Ferrón, Phys. Rev. B **35**, 2198 (1987).

[46] J. J. Vajo, R. E. Doty, and E. H. Cirlin, J. Vac. Sci. Technol. A **14**, 2709 (1996).

[47] R. Cuerno, H. A. Makse, S. Tomassone, S. T. Harrington, and H. E. Stanley, Phys. Rev. Lett. **75**, 4464 (1995).